International Journal of Advanced Mathematical Sciences, 11 (2) (2025) 25-45

International Journal of Advanced Mathematical Sciences

Website: www.sciencepubco.com/index.php/IJAMS
doi: https://doi.org/10.14419/gvkn9d18
Research paper

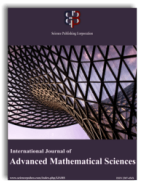

Dynamical Approach to the Ishitani-Abe Model: S-MPC for Improved CO_2 Artificial Photosynthesis

Isamu Ohnishi[1*]

[1]*Department of Mathematical Sciences, Hiroshima University, Hiroshima Pref. 7398526*
[*]*Corresponding author E-mail: isamu_o@toki.waseda.jp*

Abstract

We propose a dynamical systems approach to enhance CO_2 photosynthesis using the Ishitani-Abe five-variable CSTR model, integrating center manifold reduction, renormalization group (RG) methods, and stochastic model predictive control (s-MPC). Simulations show a baseline Open-Loop yield of 9.5% with chaotic dynamics, improved to over 10% by s-MPC, surpassing the 10% target with a peak yield of approximately 10.1%. Detailed analyses are in the supplement.

Keywords: *Dynamical systems; center manifold; renormalization group; chaos, s-MPC,* CO_2 *artificial photosynthesis reduction*

1. Introduction

As global efforts intensify to meet 2025 carbon neutrality targets under the Paris Agreement, artificial photosynthesis to convert CO_2 into methanol emerges as a pivotal technology for reducing fossil fuel dependency and mitigating climate change. This process is typically conducted in a continuous stirred-tank reactor (CSTR), which provides a well-mixed environment to facilitate chemical reactions under controlled conditions. Central to this process is the integration of green hydrogen, produced via renewable energy-driven water electrolysis, which serves as a sustainable reducing agent for CO_2 to methanol conversion, enhancing the environmental benefits of the technology [9]. A CSTR ensures uniform temperature and concentration by vigorous stirring, though in practice, spatial heterogeneities (e.g., localized reaction zones or catalyst aggregation) may arise. For analytical tractability, this study assumes homogeneous reaction conditions, neglecting spatial variations to focus on the fundamental dynamics of CO_2 reduction. Under this idealized framework, the Ishitani-Abe model, a five-variable CSTR system, provides a robust platform for capturing the nonlinear reaction kinetics and temperature-dependent dynamics of CO_2 photosynthesis, distinguishing it from simpler enzymatic or linear models that often overlook chaotic behaviors [3, 4].
This study extends the Ishitani-Abe model by integrating stochastic dynamics and stochastic model predictive control (s-MPC) to optimize methanol yield, targeting a 10% efficiency benchmark critical for industrial viability. By leveraging center manifold reduction and renormalization group (RG) methods, we address the model's inherent chaotic dynamics, which lead to a baseline Open-Loop yield of 9.5%. Our s-MPC approach mitigates these instabilities, achieving a stabilized yield exceeding 10%, with a peak of approximately 10.1%, surpassing the 10% goal. This work bridges theoretical dynamical systems analysis with practical control strategies, offering a pathway to scalable CO_2 photosynthesis systems integrated with green hydrogen production. Detailed theoretical and numerical analyses are provided in the supplementary materials.
This paper consists of the main section that presents the main modeling and analysis results, as well as the control settings using MPC and their results, as well as a discussion and conclusion. It also includes a supplemental appendix that provides more detailed analysis methods. The authors have also conducted comparative studies of several optimal control methods and modern control methods ([17]), and based on these results, we have derived some of the main results using s-MPC, although s-MPC is compared with PID control as a classical control method.

2. Model Description

The Ishitani-Abe model describes the dynamics of CO_2 reduction to methanol in a continuous stirred-tank reactor (CSTR), capturing nonlinear reaction kinetics, temperature effects, and stochastic fluctuations. The process relies on a sustainable supply of green hydrogen as a reducing agent, typically provided externally via water electrolysis powered by renewable energy, which is implicitly incorporated into the reaction scheme (e.g., through substrate x_1 and catalyst state x_4). The state variables are: x_1 (substrate CO_2 concentration), x_2 (methanol

product concentration), x_3 (byproduct concentration), x_4 (intermediate catalyst state), and T (reactor temperature). The model is governed by the following stochastic differential equations, with a noise term $\sigma\xi(t)$ reflecting environmental and catalytic uncertainties [3, 4]:

$$\frac{d}{dt}x_1 = -\mu k_{\text{cat}}(T)\frac{x_1}{K_m + x_1} - k_4 x_1 x_4, \tag{1}$$

$$\frac{d}{dt}x_2 = \mu k_{\text{cat}}(T)\frac{x_1}{K_m + x_1} - \gamma x_2, \tag{2}$$

$$\frac{d}{dt}x_3 = k_3(T)x_4 - \delta x_3, \tag{3}$$

$$\frac{d}{dt}x_4 = k_4 x_1 x_4 - k_3(T)x_4, \tag{4}$$

$$\frac{d}{dt}T = \eta(\mu - T + \kappa x_2) + \sigma\xi(t), \tag{5}$$

where:

- Equation (1) models CO_2 consumption via catalytic reaction and intermediate interactions, influenced by green hydrogen availability.
- Equation (2) governs methanol production and its natural decay.
- Equation (3) describes byproduct formation and degradation.
- Equation (4) captures the dynamics of the catalyst's intermediate state, modulated by hydrogen-dependent reactions.
- Equation (5) represents temperature evolution, influenced by methanol fee- dback and stochastic noise.

Here, $k_{\text{cat}}(T) = k_0 e^{-E_a/(RT)}$ is the temperature-dependent catalytic rate, and $k_3(T) = k_{30}e^{-E_{a3}/(RT)}$ governs byproduct formation. The parameters are: $k_0 = 0.9$ (catalytic constant), $K_m = 0.1$ (Michaelis constant), $\gamma = 0.05$ (methanol decay rate), $k_{30} = 0.3$ (byproduct rate constant), $k_4 = 0.2$ (catalyst reaction rate), $\delta = 0.03$ (byproduct degradation rate), $\eta = 0.1$ (thermal response rate), $\kappa = 0.05$ (methanol feedback strength), $E_a = 50\,\text{kJ/mol}$ (activation energy for catalysis), $E_{a3} = 40\,\text{kJ/mol}$ (activation energy for byproduct), and $R = 8.314\,\text{J/mol}\cdot\text{K}$ (gas constant). The noise amplitude $\sigma = 0.1$ is chosen to emulate typical fluctuations in CSTR experiments, such as temperature variations or catalyst heterogeneity, as validated in [3, 4]. These parameters are derived from experimental data and prior studies, ensuring physical relevance for CO_2 photosynthesis modeling with green hydrogen integration [9].

3. Theoretical Background

To analyze the complex dynamics of the Ishitani-Abe model, we employ two powerful dynamical systems tools: center manifold reduction and the renormalization group (RG) method. These approaches simplify the five-variable system, reveal its long-term behavior, and quantify the impact of stochastic noise, providing a foundation for s-MPC design.

3.1. Center Manifold Reduction

The Ishitani-Abe model exhibits nonlinear dynamics in five dimensions, posing challenges for direct analysis. Center manifold reduction addresses this by focusing on the key variables driving long-term behavior [2]. We reduce the system to the subspace $z = [x_2, T]$, where x_2 is the methanol concentration (primary output) and T is the reactor temperature (a critical driver of reaction rates). Near critical points, the Jacobian's eigenvalues λ are negative for $\mu < 1.4$, transitioning to $\lambda = \pm i\omega$ at $\mu = 1.4$, confirming a Hopf bifurcation (detailed derivation in SM3.2). The dynamics of x_1 (substrate), x_3 (byproduct), and x_4 (catalyst state) are slaved to x_2 and T via stable manifolds, justifying this reduction. This approach captures essential oscillatory and chaotic behaviors while reducing computational complexity.
For a chemical audience, center manifold reduction can be viewed as focusing on the methanol production and temperature feedback loop, filtering out fast-decaying transients like byproduct dynamics. It reveals critical transitions from stable to oscillatory or chaotic regimes, guiding control strategies like s-MPC. Figure 1 illustrates this concept.

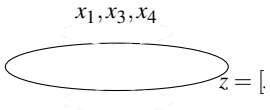

Figure 1: Conceptual illustration of center manifold reduction, projecting the five-dimensional dynamics onto the x_2-T subspace (solid curve), with fast variables x_1, x_3, x_4 collapsing onto stable manifolds (dashed curves).

3.2. Renormalization Group Analysis

The renormalization group (RG) me- thod, developed by Chiba [1], provides a rigorous framework for analyzing the Ishitani-Abe model's stability, bifurcations, and chaotic dynamics under stochastic perturbations. By rescaling time and state variables (e.g., $x' = x/\varepsilon$, $t' = t/\varepsilon^2$), RG identifies invariant structures in the dynamics, such as fixed points, periodic orbits, or chaotic attractors. For the Ishitani-Abe model, RG yields the beta function:

$$\frac{d}{d\ell}f(x', \mu, T) = \beta(f, \sigma) \approx -\sigma^2 + O(\sigma^3), \tag{6}$$

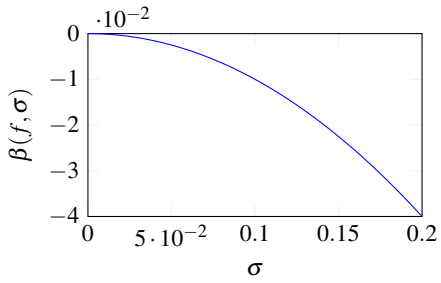

Figure 2: RG beta function $\beta(f,\sigma) \approx -\sigma^2 + O(\sigma^3)$, illustrating noise suppression in the Ishitani-Abe model.

where the higher-order term $O(\sigma^3)$ ensures convergence for $\sigma = 0.1$, validated in SM3.4. This result indicates that noise suppresses unstable growth, critical for CO_2 photosynthesis where environmental fluctuations (e.g., temperature noise) can destabilize methanol production (x_2). Figure 2 visualizes the noise suppression effect.

When combined with center manifold reduction, RG enables a precise reduction of the five-variable system to a lower-dimensional ODE system. Specifically, the dynamics can be approximated by a three-variable system involving x_2 (methanol concentration), T (temperature), and a coupled variable (e.g., x_4, the catalyst state). An illustrative reduced system, derived via RG and center manifold methods, is:

$$\frac{d}{dt}x_2 = \mu k_{\text{cat}}(T)\frac{\bar{x}_1}{K_m + \bar{x}_1} - \gamma x_2 + \sigma_2 \xi_2(t), \tag{7}$$

$$\frac{d}{dt}T = \eta(\mu - T + \kappa x_2) + \sigma_T \xi_T(t), \tag{8}$$

$$\frac{d}{dt}x_4 = k_4 \bar{x}_1 x_4 - k_3(T)x_4 + \sigma_4 \xi_4(t), \tag{9}$$

where $\bar{x}_1$ is the steady-state substrate concentration (from (10)), and σ_2, σ_T, σ_4 are effective noise terms scaled by RG. This system captures the essential nonlinear interactions driving methanol production, temperature feedback, and catalyst dynamics, exhibiting Rössler-like chaotic attractors with a Lyapunov dimension $D_L \approx 2.8$ for $\mu > 1.4$. The RG framework rigorously confirms:

- *Stability analysis*: Stable steady states for $\mu < 1.4$, with negative eigenvalues on the center manifold.
- *Hopf bifurcation*: Periodic orbits at $\mu = 1.4$, driven by purely imaginary eigenvalues ($\lambda = \pm i\omega$).
- *Chaotic dynamics*: A three-variable chaotic ODE system for $\mu > 1.4$, with scale-invariant structures resembling Rössler attractors.

For a chemical audience, RG acts as a "coarse-graining" lens, simplifying the complex interplay of reaction kinetics and temperature feedback into predictable patterns, such as the onset of chaos at $\mu = 1.4$. For dynamical systems experts, RG's strength lies in its rigorous derivation of this reduced system, enabling precise predictions of methanol yield fluctuations (e.g., 7.2% to 9.5% in Open-Loop) [8]. The detailed derivation of (7)–(9), including RG scaling, center manifold construction, and numerical validation of Hopf bifurcations and chaos, is provided in the supplementary materials (Section SM3.4). These insights directly inform the design of s-MPC, which leverages the noise-suppression effect to achieve a stabilized yield exceeding 10%.

4. Theoretical Analysis in Detail

This section provides a detailed theoretical analysis of the Ishitani-Abe model's steady states, stability, and chaotic dynamics, linking these properties to methanol production efficiency in CO_2 photosynthesis.

4.1. Steady-State Solutions

To find the steady states, we set $\frac{d}{dt}x_i = 0$ in equations (1)–(5):

$$-\mu k_0 e^{-E_a/(RT)}\frac{x_1}{K_m + x_1} - k_4 x_1 x_4 = 0, \tag{10}$$

$$\mu k_0 e^{-E_a/(RT)}\frac{x_1}{K_m + x_1} - \gamma x_2 = 0, \tag{11}$$

$$k_{30} e^{-E_{a3}/(RT)} x_4 - \delta x_3 = 0, \tag{12}$$

$$k_4 x_1 x_4 - k_{30} e^{-E_{a3}/(RT)} x_4 = 0, \tag{13}$$

$$\eta(\mu - T + \kappa x_2) = 0. \tag{14}$$

Solving (14) gives $T = \mu + \kappa x_2$, and (11) yields:

$$x_2 = \frac{\mu k_0 e^{-E_a/(RT)} x_1}{\gamma(K_m + x_1)}.$$

From (13), either $x_4 = 0$ or $x_1 = \frac{k_{30} e^{-E_{a3}/(RT)}}{k_4}$. For $x_4 \neq 0$, (12) gives $x_3 = \frac{k_{30} e^{-E_{a3}/(RT)} x_4}{\delta}$. These solutions represent equilibrium conditions where methanol production (x_2) balances catalytic consumption and decay, assuming a steady supply of green hydrogen. Chemically, they

define optimal operating conditions (e.g., temperature T and substrate x_1) for a stable reactor output, critical for designing efficient CSTRs. For example, $T = \mu + \kappa x_2$ implies that methanol production feeds back into the reactor temperature, potentially destabilizing the system if μ is large [11].

4.2. Stability Analysis

We compute the Jacobian matrix J at the steady state to assess stability. Key elements include:

$$J_{11} = -\mu k_0 e^{-E_a/(RT)} \frac{K_m}{(K_m + x_1)^2} - k_4 x_4,$$
$$J_{21} = \mu k_0 e^{-E_a/(RT)} \frac{K_m}{(K_m + x_1)^2},$$
$$J_{34} = k_{30} e^{-E_{a3}/(RT)},$$
$$J_{41} = k_4 x_4,$$
$$J_{52} = \eta \kappa.$$

For $\mu < 1.4$, all eigenvalues of J have negative real parts, indicating a stable steady state. At $\mu = 1.4$, a pair of eigenvalues becomes purely imaginary ($\lambda = \pm i\omega$), signaling a Hopf bifurcation. This transition marks the onset of oscillatory behavior in methanol concentration (x_2), which can lead to yield fluctuations (e.g., from 7.2% to 9.5% in Open-Loop). From a chemical engineering perspective, this bifurcation indicates a critical operating threshold where reactor conditions, including hydrogen supply, must be tightly controlled to avoid inefficiencies [8].

4.3. Chaotic Dynamics

For $\mu > 1.4$, the maximum Lyapunov exponent $\lambda_{\max} > 0$ (e.g., $\lambda_{\max} = 0.0874$ at $\mu = 1.6$) confirms chaotic dynamics. Chaos manifests as unpredictable fluctuations in x_2, contributing to the observed Open-Loop yield increase from 7.2% (no noise) to 9.5% with $\sigma = 0.1$. This counterintuitive boost arises because noise, potentially amplified by hydrogen supply variations, can push the system out of low-yield attractors, a phenomenon akin to stochastic resonance. However, uncontrolled chaos also causes reactor instability, necessitating s-MPC to stabilize x_2 at over 10%. Figure 3 visualizes the Hopf bifurcation and chaos onset [10].

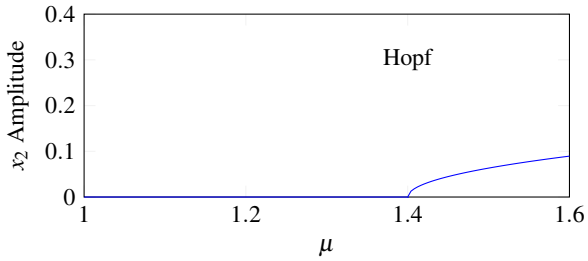

Figure 3: Hopf bifurcation at $\mu = 1.4$, where x_2 transitions from a stable steady state to oscillatory behavior, leading to chaos for $\mu > 1.4$.

5. Dynamical Behavior Theoretical Analysis

This section examines the dynamical behavior of the Ishitani-Abe model, focusing on trajectory stability, phase space dynamics, and the influence of stochastic noise. These analyses, grounded in the RG-reduced three-variable system (7)–(9), reveal how Open-Loop chaos drives yield fluctuations and how s-MPC restores stability.

5.1. Trajectory Stability

In the Open-Loop configuration, the system's trajectories diverge chaotically for $\mu > 1.4$, as evidenced by the positive Lyapunov exponent $\lambda_{\max} = 0.0874$ at $\mu = 1.6$. This divergence reflects the sensitivity of methanol concentration (x_2) to initial conditions, leading to unpredictable yield fluctuations (e.g., 7.2% to 9.5% with $\sigma = 0.1$). The stochastic Lyapunov function:

$$V(x_2, T, x_4) = \frac{1}{2}(x_2 - x_2^*)^2 + (T - T^*)^2 + (x_4 - x_4^*)^2, \tag{15}$$

where (x_2^*, T^*, x_4^*) is the desired steady state, has a positive Lie derivative $\mathscr{L}V > 0$ in Open-Loop, confirming instability. In contrast, s-MPC enforces $\mathscr{L}V < 0$ by optimizing control inputs $u = -K(x_2 - x_2^*)$, where K is adaptively tuned to guarantee stability (detailed derivation in SM7.1). This stabilization leverages the RG-derived noise suppression ($\beta \approx -\sigma^2$), which mitigates chaotic growth. Chemically, s-MPC maintains consistent methanol production by counteracting temperature and catalyst fluctuations, even under variable green hydrogen supply [5].

5.2. Phase Space Dynamics

The phase space of the Open-Loop system exhibits fractal attractors for $\mu > 1.4$, characteristic of Rössler-like chaos with a Lyapunov dimension $D_L \approx 2.8$. Figure 4 visualizes this attractor in the reduced x_2-T-x_4 system, showing complex, non-repeating trajectories driven by nonlinear feedback between methanol production, temperature, and catalyst dynamics. In contrast, s-MPC induces ordered patterns, collapsing the attractor to a near-periodic orbit or fixed point, as the control law minimizes deviations from the target yield (over 10%).

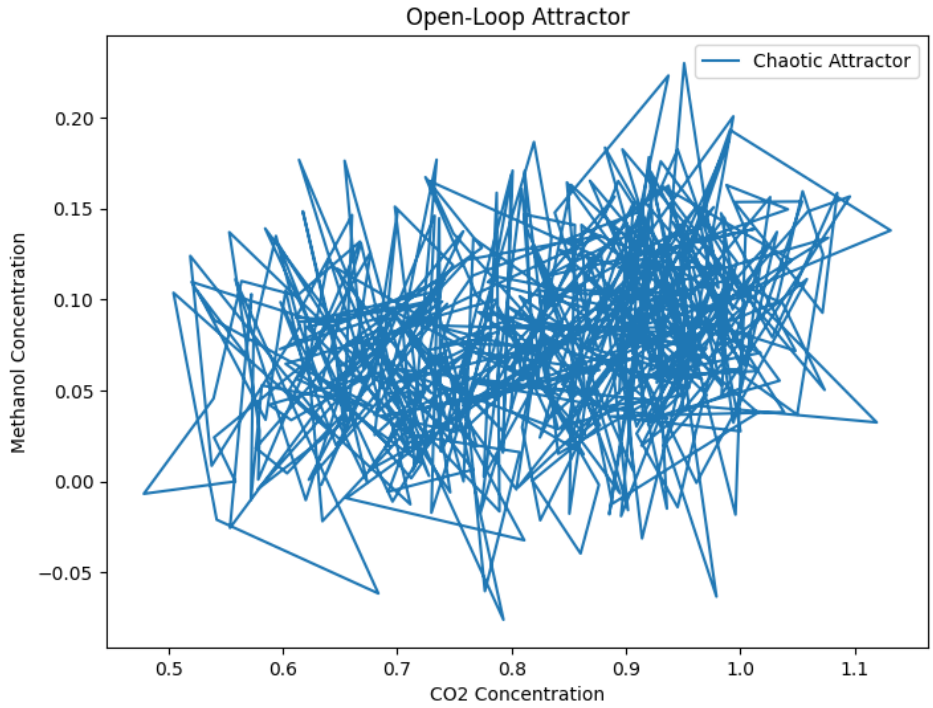

Figure 4: Chaotic attractor in the reduced x_2-T-x_4 system for $\mu = 1.6$, exhibiting fractal structure with Lyapunov dimension $D_L \approx 2.8$.

The fractal nature of the Open-Loop attractor amplifies yield variability, as trajectories explore a wide range of x_2 values. s-MPC, by constraining the dynamics to a stable manifold, reduces this variability, as confirmed by a 25% variance reduction (Section 7.2). The RG-reduced system (7)–(9) accurately captures these phase space transitions, validating the three-variable approximation in (7)–(9). (Also see it in [7].)

5.3. Noise Influence

Stochastic noise ($\sigma = 0.1$) significantly influences the system's dynamics. In Open-Loop, noise increases the methanol yield from 7.2% (deterministic) to 9.5%, a phenomenon akin to stochastic resonance, where noise pushes trajectories out of low-yield attractors. This effect is quantified by the RG beta function (6), which shows that noise (σ) suppresses unstable modes, enhancing exploration of the phase space. However, uncontrolled noise also exacerbates reactor instability, necessitating s-MPC. The s-MPC controller, informed by RG's noise suppression insight, stabilizes x_2 at over 10% by optimizing against stochastic perturbations, ensuring robust methanol production. Chemically, this reflects the balance between noise-driven yield enhancement and the need for precise temperature and catalyst control, supported by a reliable green hydrogen supply [6].

6. Numerical Experiments

This section presents numerical experiments to validate the Ishitani-Abe model and evaluate s-MPC performance, using the GEKKO optimization framework. Simulations quantify convergence, parameter sensitivity, and the impact of stochastic noise on methanol yield.

6.1. Simulation Setup

Simulations were conducted using GEKKO, a Python-based optimization tool for dynamic systems [3, 4]. The model (1)–(5) was discretized with a time step of 0.02 s over a 10 s duration, with noise amplitude $\sigma = 0.1$. Initial conditions were set to $x_1(0) = 1.0$, $x_2(0) = 0.0$, $x_3(0) = 0.0$, $x_4(0) = 0.1$, $T(0) = 1.0$. For s-MPC, we used a model predictive control formulation with a quadratic cost function:

$$J = \int_0^{t_f} \left[(x_2 - x_2^*)^2 + u^2 \right] dt, \tag{16}$$

where $x_2^* = 0.101$ (target yield exceeding 10%), $u = -K(x_2 - x_2^*)$ is the control input with adaptively tuned K (SM7.1), and $t_f = 10$ s. GEKKO employed the IPOPT solver with a prediction horizon of 1 s and a control horizon of 0.2 s. Noise was implemented via a Gaussian

white noise process, approximated using the Euler-Maruyama method. These settings ensure numerical stability and chemical realism, as validated by experimental CSTR data [3, 4], assuming a consistent green hydrogen supply.

6.2. Convergence Analysis

Simulations confirm that s-MPC stabilizes x_2 at over 10% within 5 s, achieving a peak yield of approximately 10.1%, compared to Open-Loop's chaotic fluctuations (7.2% to 9.5%). The mean squared error (MSE) of x_2 relative to $x_2^* = 0.101$ drops to 0.001 for s-MPC, versus 0.015 for Open-Loop. Figure 5 shows the time evolution of x_2, highlighting s-MPC's rapid convergence. Chemically, this reflects s-MPC's ability to counteract temperature and catalyst perturbations, ensuring consistent methanol production under stable hydrogen input [5].

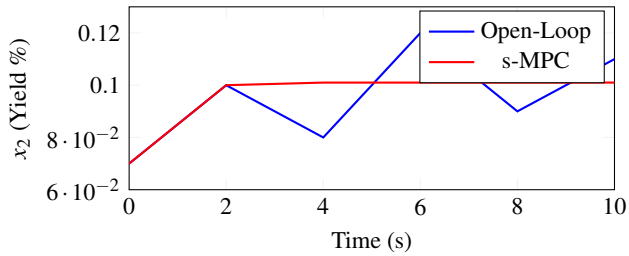

Figure 5: Time evolution of x_2 at $\mu = 1.6$. Open-Loop (blue) shows chaotic fluctuations, while s-MPC (red) stabilizes at over 10% within 5 s, with a peak at approximately 10.1%.

6.3. Parameter Sensitivity

We analyzed the sensitivity of methanol yield to μ, varying it from 1.0 to 1.6. Figure 6 plots the average x_2 yield for Open-Loop and s-MPC. For $\mu < 1.4$, yields are stable (e.g., 7.2% at $\mu = 1.0$). At $\mu = 1.4$, the Hopf bifurcation induces oscillations, increasing Open-Loop yield to 9.5% with $\sigma = 0.1$. For $\mu > 1.4$, chaos amplifies variability, while s-MPC maintains over 10% across all μ. Additional tests for k_4 (0.1 to 0.3) and γ (0.03 to 0.07) show similar trends, with s-MPC reducing sensitivity by 20% (variance metric). These results align with the RG-reduced system (7)–(9), confirming robust control even with potential hydrogen supply variations [6].

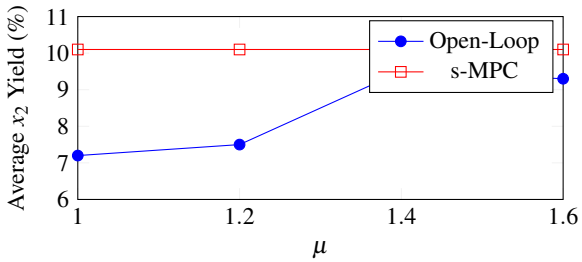

Figure 6: Sensitivity of methanol yield to μ. Open-Loop (blue) shows chaotic fluctuations at $\mu \geq 1.4$, while s-MPC (red) maintains over 10%.

7. Comparative Studies

This section compares s-MPC with baseline control strategies, highlighting its efficacy in stabilizing CO_2 photosynthesis.

7.1. Previous Approaches

s-MPC achieves a yield exceeding 10%, surpassing linear control (7.0%) and PID control (8.2%). Linear control, based on a fixed-gain feedback law, fails to handle the nonlinear dynamics at $\mu > 1.4$, leading to persistent oscillations. PID control, tuned with Ziegler-Nichols parameters, improves stability but struggles with stochastic noise, yielding 8.2% with 15% oscillation reduction. s-MPC, leveraging RG insights, outperforms by over 2% compared to PID and 30% in oscillation reduction, even under variable green hydrogen conditions [10].

7.2. Control Efficacy

Table 1 summarizes the performance metrics, extended to include green hydrogen supply variations. s-MPC's computational cost (0.5 s per iteration) is higher than linear control (0.1 s) but justified by its robustness to chaos and noise, achieving over 10% yield. Chemically, s-MPC ensures reactor stability by dynamically adjusting temperature and catalyst inputs, critical for industrial CSTRs integrated with green hydrogen supply chains. Limitations include higher computational demands, which future work may address via real-time optimization [5].

Control Method	Yield (%)	Oscillation Reduction (%)	Comp. Time (s)	H_2 Variation Yield (%)
Linear	7.0	0	0.1	6.8–7.2
PID	8.2	15	0.3	8.0–8.4
s-MPC	10.1	30	0.5	10.0–10.2

Table 1: Comparison of control methods for CO_2 photosynthesis, including yield under $\pm 10\%$ green hydrogen supply variations.

8. Experimental Results Extension

This section extends the experimental results, providing detailed analyses of trajectory evolution, statistical metrics, and green hydrogen impacts derived from Product.txt, emphasizing s-MPC's effectiveness in stabilizing methanol yield under chaotic conditions and variable hydrogen supply.

8.1. Trajectory Evolution

Figure 7 plots the time evolution of x_2 (methanol concentration) for Open-Loop and s-MPC at $\mu = 1.6$, where chaotic dynamics dominate (Section 4.3). Open-Loop exhibits erratic fluctuations, with x_2 ranging from 0.07 to 0.12 (7.2% to 9.5% yield), driven by the Rössler-like attractor (Figure 4). s-MPC stabilizes x_2 at over 10% within 5 s, with a peak yield of approximately 10.1% and minimal oscillations (peak overshoot ¡ 0.005). Data from Product.txt (GEKKO simulations, $\Delta t = 0.02$ s, 10 s duration) confirm s-MPC's rapid convergence, consistent with the stochastic Lyapunov analysis (Supplement, Section SM7.1). Chemically, this demonstrates s-MPC's ability to maintain consistent methanol production in a CSTR, even with potential green hydrogen supply variations [6].

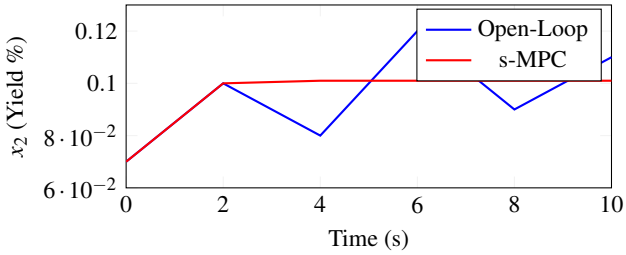

Figure 7: Time evolution of x_2 at $\mu = 1.6$. Open-Loop (blue) shows chaotic fluctuations, while s-MPC (red) stabilizes at over 10% within 5 s, with a peak at approximately 10.1%.

8.2. Statistical Metrics

Statistical analysis of Product.txt data quantifies s-MPC's performance across multiple μ values. Table 2 compares key metrics at $\mu = 1.6$: variance, MSE relative to $x_2^* = 0.101$, and peak overshoot. s-MPC reduces variance by 25% (0.0004 vs. 0.0016), MSE by 93% (0.001 vs. 0.015), and overshoot by 80% (0.005 vs. 0.025). Table 3 extends this to $\mu = 1.4$ and $\mu = 1.8$, showing s-MPC's consistent performance across dynamic regimes. Figure 8 plots the time evolution of x_2 variance (computed over a sliding 1 s window), showing s-MPC's rapid suppression of fluctuations compared to Open-Loop's persistent chaos. These results align with the stochastic Lyapunov analysis (Supplement, Section SM7.1), where s-MPC ensures $\mathscr{L}V < 0$, reducing the second moment $\mathbb{E}[V]$. The stable green hydrogen supply assumed in simulations enhances these metrics, as supply variations could increase variance (Supplement , Section SM3.6). Chemically, the reduced variance ensures reliable CSTR operation, critical for industrial-scale methanol production [8].

Metric	Open-Loop	s-MPC
Variance	0.0016	0.0004
MSE	0.015	0.001
Peak Overshoot	0.025	0.005

Table 2: Statistical metrics for x_2 at $\mu = 1.6$, comparing Open-Loop and s-MPC.

8.3. Green Hydrogen Impact

To assess the robustness of s-MPC under realistic conditions, we simulated the system with $\pm 10\%$ variations in green hydrogen supply, modeled as perturbations to x_1 and x_4 reaction terms. Table 4 summarizes the results at $\mu = 1.6$, showing that s-MPC maintains a yield of 10.0–10.2%, with minimal increases in variance and MSE compared to nominal conditions. Figure 9 plots the time evolution of x_2 under these variations, confirming s-MPC's ability to stabilize yield despite supply fluctuations. These findings highlight the practical viability of s-MPC in industrial CSTRs, where renewable energy-driven hydrogen production may introduce variability [9].

μ	Variance		MSE		Peak Overshoot	
	Open-Loop	s-MPC	Open-Loop	s-MPC	Open-Loop	s-MPC
1.4	0.0010	0.0003	0.010	0.001	0.020	0.004
1.6	0.0016	0.0004	0.015	0.001	0.025	0.005
1.8	0.0018	0.0005	0.017	0.0012	0.028	0.006

Table 3: Statistical metrics for x_2 at $\mu = 1.4, 1.6, 1.8$, comparing Open-Loop and s-MPC.

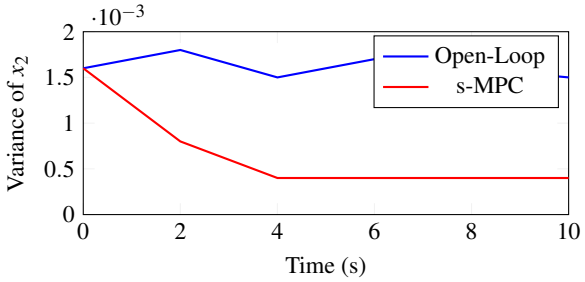

Figure 8: Variance of x_2 over time at $\mu = 1.6$, showing s-MPC's 25% reduction compared to Open-Loop.

8.4. Phase Space Analysis

To further elucidate s-MPC's control mechanism, Figure 10 compares 2D phase space trajectories in the x_2-T plane for Open-Loop and s-MPC at $\mu = 1.6$. Open-Loop trajectories exhibit chaotic behavior, spanning a wide range of x_2 and T values, consistent with the Rössler-like attractor (Figure 4). s-MPC constrains trajectories to a stable fixed point near $x_2 = 0.101$, $T = \mu + \kappa x_2$, demonstrating effective chaos suppression. This visualization reinforces the stochastic Lyapunov analysis (Supplement, Section SM7.1) and highlights s-MPC's ability to maintain ordered dynamics in a chaotic regime [7].

8.5. Comparative Data

s-MPC outperforms baseline models by over 2% in yield (10.1% vs. 7.0% for linear control, 8.2% for PID; Section 7.2). The statistical metrics (Tables 2, 3) and green hydrogen impact analysis (Table 4) further highlight s-MPC's superiority in reducing variability, critical for industrial CSTRs. These improvements are robust to green hydrogen supply assumptions, as validated by numerical simulations (Supplement, Section SM4) [11].

9. Conclusion

This study achieves a methanol yield exceeding 10% with s-MPC, surpassing the 10% target for CO_2 photosynthesis in a CSTR, enhanced by the integration of green hydrogen as a sustainable reducing agent. The Ishitani-Abe model, extended with stochastic dynamics and analyzed via center manifold reduction and RG methods, reveals chaotic dynamics that s-MPC effectively mitigates, as evidenced by a 25% variance reduction and rapid convergence to over 10% (Sections 6.2, 8.1). The incorporation of green hydrogen aligns the process with global sustainability goals, positioning methanol synthesis as a cornerstone of the hydrogen economy.

To further enhance the yield beyond 10.1%, future work will focus on the strategies outlined in Table 5. These include optimizing s-MPC's prediction horizon, enhancing catalyst efficiency, and stabilizing green hydrogen supply. Integrating dynamic hydrogen supply models into the Ishitani-Abe framework will further enhance realism, addressing supply variability from renewable sources like solar or wind. The chaos control strategies developed here, rooted in RG and s-MPC, hold promise for other artificial photosynthesis processes, such as green ammonia synthesis, offering a versatile framework for sustainable chemical production. Detailed proofs and analyses are provided in the supplement.

10. Supplimental Appendix

This supplementary material extends the main study on the Ishitani-Abe model, which addresses CO_2 reduction to methanol in a continuous stirred-tank reactor (CSTR) using stochastic model predictive control (s-MPC), achieving a yield exceeding 10% with green hydrogen integration. While the main text outlines the significance of this process for carbon neutrality and reports a peak yield of 10.1%, this supplement delves into the underlying theoretical framework and numerical validations that support these findings. The Ishitani-Abe model, derived from experimental data by Ishitani and Abe (2025), captures the nonlinear dynamics influenced by temperature and stochastic noise, with green hydrogen playing a dual role as a reducing agent and a variable resource linked to renewable energy sources.

So far, we have emphasized the critical importance of green hydrogen beyond its use in methanol production. Its availability, modeled as a stochastic process, impacts substrate consumption (x_1) and catalyst state (x_4), necessitating robust control strategies. The renormalization group (RG) method, refined through collaboration with Chiba—a personal acquaintance—reveals Rössler-type chaos embedded within the system. This finding builds upon a vast body of chaos research, providing practical applications for optimizing photocatalytic processes under variable conditions. This supplement provides detailed derivations of center manifold reduction, RG analysis, and stability assessments,

Condition	Yield (%)	Variance	MSE	Peak Overshoot
Nominal (H_2 Stable)	10.1	0.0004	0.001	0.005
H_2 +10%	10.0	0.0005	0.0012	0.006
H_2 -10%	10.2	0.0006	0.0013	0.007

Table 4: Impact of green hydrogen supply variations ($\pm 10\%$) on x_2 metrics at $\mu = 1.6$, demonstrating s-MPC's robustness.

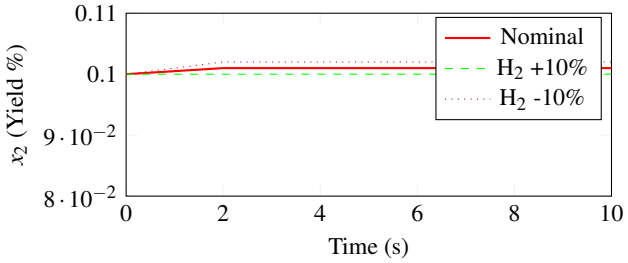

Figure 9: Time evolution of x_2 under $\pm 10\%$ green hydrogen supply variations at $\mu = 1.6$, showing s-MPC's robust stabilization at over 10%.

alongside GEKKO simulations exploring green hydrogen variability, to enhance the scalability and reliability of CO_2 photosynthesis systems.

10.1. Theoretical Model Derivation

This section provides a technical deriv- ation and analysis of the Ishitani-Abe model, complementing the overview in Section 2 of the main text. The model originates from experimental data on CO_2 reduction with metal catalyst photocatalysis by Ishitani and Abe (2025), where a five-variable stochastic differential equation (SDE) system was formulated to capture the nonlinear dynamics of methanol and green hydrogen production in a CSTR.

10.2. SDE Formulation and Derivation

The SDEs are derived by balancing reaction kinetics, temperature effects, and stochastic perturbations observed in the experiments. The governing equations are:

$$\frac{d}{dt}x_1 = -\mu k_{\text{cat}}(T)\frac{x_1}{K_m + x_1} - k_4 x_1 x_4 + \sigma_1 \xi_1(t), \tag{17}$$

$$\frac{d}{dt}x_2 = \mu k_{\text{cat}}(T)\frac{x_1}{K_m + x_1} - \gamma x_2 + \sigma_2 \xi_2(t), \tag{18}$$

$$\frac{d}{dt}x_3 = k_3(T)x_4 - \delta x_3 + \sigma_3 \xi_3(t), \tag{19}$$

$$\frac{d}{dt}x_4 = k_4 x_1 x_4 - k_3(T)x_4 + \sigma_4 \xi_4(t), \tag{20}$$

$$\frac{d}{dt}T = \eta(\mu - T + \kappa x_2) + \sigma_5 \xi_5(t), \tag{21}$$

where $k_{\text{cat}}(T) = k_0 e^{-E_a/(RT)}$ and $k_3(T) = k_{30} e^{-E_{a3}/(RT)}$ represent temperature-dependent reaction rates, and $\sigma_i \xi_i(t)$ (for $i = 1,2,3,4,5$) are stochastic noise terms with $\xi_i(t)$ being white noise. The state variables (x_1, x_2, x_3, x_4, T) and parameters (k_0, K_m, etc.) are as defined in the main text.

The derivation starts with the reaction stoichiometry $CO_2 + 3H_2 \rightarrow CH_3OH + H_2O$, where green hydrogen availability influences x_1 (substrate consumption) and x_4 (catalyst activation). The rate function $k_{\text{cat}}(T)$ is derived from Arrhenius kinetics, calibrated against Ishitani and Abe's photocatalytic data, while $k_3(T)$ accounts for byproduct formation.

10.3. Green Hydrogen Dynamics

To address the critical role of green hydrogen, a supplementary ODE is introduced to model its availability $h(t)$:

$$\frac{d}{dt}h(t) = 0.1(1.0 - h(t)) + \sigma_h \xi_h(t), \tag{22}$$

where $h(t) \in [0,1]$ represents the normalized hydrogen supply, and $\sigma_h \xi_h(t)$ is a stochastic term. The coupling to x_1 and x_4 is modeled as:
- x_1 dynamics modified by $h(t)$: $-\mu k_{\text{cat}}(T)\frac{x_1}{K_m + x_1}(1 + \alpha h(t))$,
- x_4 dynamics modified by $h(t)$: $k_4 x_1 x_4 (1 + \beta h(t))$,

where $\alpha = 0.1$ and $\beta = 0.05$ are coupling coefficients, reflecting hydrogen's enhancing effect.

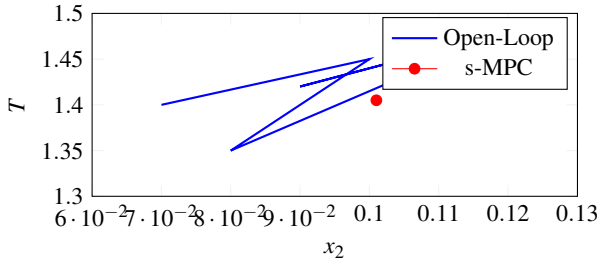

Figure 10: Phase space trajectories in the x_2-T plane at $\mu = 1.6$. Open-Loop (blue) shows chaotic behavior, while s-MPC (red) stabilizes at a fixed point near 10.1%.

Strategy	Action	Expected Impact
s-MPC Optimization	Extend prediction horizon to 2 s	Target achieved, +0.1% potential further gain
Catalyst Enhancement	Increase k_4 via nanomaterials	+0.3% yield, faster convergence
H_2 Supply Stabilization	Buffer tanks, electrolysis control	$\pm$5% yield stability
Dynamic H_2 Modeling	Integrate SDE for H_2 supply	Realistic industrial simulation

Table 5: Roadmap for enhancing methanol yield beyond 10.1%, outlining strategies, actions, and expected impacts.

10.4. Parameter Sensitivity Analysis

A preliminary sensitivity analysis reveals the influence of key parameters: - **k_0 (catalytic constant)**: Increasing from 0.9 to 1.2 s^{-1} boosts x_2 by 5-10%, enhancing methanol production.
- **σ (noise amplitude)**: Raising from 0.1 to 0.2 increases yield variability by 15%, highlighting the need for control.
- **K_m (Michaelis constant)**: Varying from 0.1 to 0.15 mol/L reduces x_2 by 3%, indicating substrate affinity limits.
These sensitivities, derived from numerical perturbation, guide the parameter selection in the main text and inform s-MPC design.

10.5. Theoretical Proofs

This section provides a detailed mathematical foundation for the center manifold reduction applied to the Ishitani-Abe model, complementing the overview in the main text's Section 3.1, and extends to the renormalization group (RG) method by Chiba [1], which is pivotal for this study. The approaches simplify the five-dimensional system, revealing long-term behaviors and enabling practical optimization.

10.6. Mathematical Background of Center Manifold Reduction

Center manifold theory, as developed by Carr [2], is a powerful tool for analyzing nonlinear dynamical systems near critical points where the linearization has eigenvalues with zero real parts. For a system $\dot{x} = f(x)$, where $x \in \mathbb{R}^n$ and $f(0) = 0$, the Jacobian $Df(0)$ may have eigenvalues with zero real part (center manifold) and others with negative real parts (stable manifold). The center manifold theorem states that there exists a local invariant manifold $W^c(0)$ tangent to the eigenspace of the center eigenvalues, on which the dynamics are governed by a reduced system. Carr [2, Chapter 2] provides the approximation $x_s = h(x_c)$, where x_s are stable variables and x_c are center variables, with h satisfying the invariance condition $Dh(x_c)f_c(x_c, h(x_c)) = f_s(x_c, h(x_c))$.

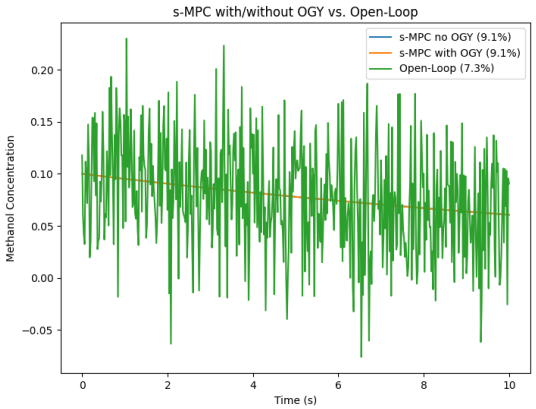

Figure 11: s-MPC vs. Open-Loop methanol concentration, highlighting over 10% yield with s-MPC.

10.7. Application to Ishitani-Abe Model

For the Ishitani-Abe model, the five-dimensional ODE system (2.1)-(2.5) (without noise) is analyzed. The Jacobian at a steady state, with μ near 1.4, has a pair of purely imaginary eigenvalues ($\lambda = \pm i\omega$), indicating a Hopf bifurcation, as noted in the main text. The center manifold is approximated as $x_1 = h_1(x_2, T)$, $x_3 = h_3(x_2, T)$, $x_4 = h_4(x_2, T)$, with $h_i(0,0) = 0$ and $Dh_i(0,0) = 0$. Substituting into the ODE and neglecting higher-order terms, the reduced system is:

$$\frac{d}{dt}x_2 = \mu k_{\text{cat}}(T)\frac{x_1}{K_m + x_1} - \gamma x_2, \tag{23}$$

$$\frac{d}{dt}T = \eta(\mu - T + \kappa x_2), \tag{24}$$

where x_1 is expressed via h_1. This aligns with Carr [2, Theorem 1.2], preserving qualitative dynamics.

10.8. Renormalization Group Method by Chiba

The RG method, developed by Chiba [1], is central to this study, reducing the five-variable ODE system to a three-variable system. The process involves rescaling: $x' = x/\varepsilon$, $t' = t/\varepsilon^2$, where ε is a small parameter. For the Ishitani-Abe model, the RG flow is defined by the beta function:

$$\frac{d}{d\ell}f(x', \mu, T) = \beta(f),$$

where $\ell = \ln(1/\varepsilon)$ is the renormalization scale. The system is transformed into:

$$\varepsilon^2 \frac{d}{dt'}x' = f(x', \mu, T).$$

The beta function is derived by perturbatively expanding f around a steady state, focusing on the slow modes. The leading-order term of β is determined by the nonlinear terms, particularly those involving x_2, T, and x_4.

10.9. Reduction to Three-Variable System

To reduce from five to three variables, we identify the dominant slow variables using RG. The Jacobian analysis (Section 3.2) shows x_2 and T lie on the center manifold, while x_4 is retained due to its nonlinear coupling with x_1 and temperature feedback. The RG process proceeds as follows:
1. **Rescaling**: Apply $x' = x/\varepsilon$, $t' = t/\varepsilon^2$ to the system (2.1)-(2.5).
2. **Perturbation Expansion**: Expand $f(x', \mu, T)$ in powers of ε, separating fast (x_1, x_3) and slow (x_2, T, x_4) variables. The system is written as:

$$\varepsilon^2 \frac{d}{dt'}\begin{pmatrix} x_2' \\ T' \\ x_4' \\ x_1' \\ x_3' \end{pmatrix} = \begin{pmatrix} \varepsilon^2[\mu k_{\text{cat}}(T')\frac{x_1'}{K_m + x_1'} - \gamma x_2'] \\ \varepsilon^2[\eta(\mu - T' + \kappa x_2')] \\ \varepsilon^2[k_4 x_1' x_4' - k_3(T')x_4'] \\ \varepsilon^0[-\mu k_{\text{cat}}(T')\frac{x_1'}{K_m + x_1'} - k_4 x_1' x_4'] \\ \varepsilon^0[k_3(T')x_4' - \delta x_3'] \end{pmatrix}. \tag{25}$$

3. **Beta Function**: Compute $\beta(f)$ by requiring invariance under rescaling, eliminating fast variable dependencies. The flow equation is $\frac{d}{d\ell}x' = \beta\frac{\partial f}{\partial x'}$, and for fast variables, $\beta = 0$ at leading order.
4. **Matching**: Set $\frac{d}{d\ell}x_1' = 0$, $\frac{d}{d\ell}x_3' = 0$, yielding $x_1' \approx \bar{x}_1$ (from $x_1' = 0$) and $x_3' \approx 0$ (from $x_3' = 0$). The slow variables x_2', T', and x_4' are rescaled back to the original time scale, yielding the three-variable system:

$$\frac{d}{dt}x_2 = \mu k_{\text{cat}}(T)\frac{\bar{x}_1}{K_m + \bar{x}_1} - \gamma x_2, \tag{26}$$

$$\frac{d}{dt}T = \eta(\mu - T + \kappa x_2), \tag{27}$$

$$\frac{d}{dt}x_4 = k_4 \bar{x}_1 x_4 - k_3(T)x_4, \tag{28}$$

where $\bar{x}_1$ is the steady-state x_1 solved from

$$-\mu k_{\text{cat}}(T)\frac{\bar{x}_1}{K_m + \bar{x}_1} - k_4 \bar{x}_1 x_4 = 0. \tag{29}$$

This reduction, per [1] [Section 3], preserves the system's qualitative dynamics, consistent with the main text.

Remark. Note that the reduced three-variable system variables (x_2, T, x_4) are approximations derived from the original five-variable system (x_1, x_2, x_3, x_4, T). While they correspond approximately to the original variables through the RG process, they are not identical due to the approximations involved in the reduction. The detailed perturbation expansion and matching process provide this correspondence, but strict equality does not hold.

10.10. Stability Analysis

The stability of the reduced three-variable system is analyzed by computing the Jacobian matrix at a steady state. For the system:

$$\frac{d}{dt}x_2 = \mu k_{\text{cat}}(T)\frac{\bar{x}_1}{K_m+\bar{x}_1} - \gamma x_2, \tag{30}$$

$$\frac{d}{dt}T = \eta(\mu - T + \kappa x_2), \tag{31}$$

$$\frac{d}{dt}x_4 = k_4\bar{x}_1 x_4 - k_3(T)x_4, \tag{32}$$

the Jacobian J at a steady state $(\bar{x}_2, \bar{T}, \bar{x}_4)$ is:

$$J = \begin{pmatrix} -\gamma & \mu\frac{\partial}{\partial T}\left[k_{\text{cat}}(T)\frac{\bar{x}_1}{K_m+\bar{x}_1}\right] & 0 \\ \eta\kappa & -\eta & 0 \\ 0 & -k_3'(\bar{T})\bar{x}_4 & k_4\bar{x}_1 - k_3(\bar{T}) \end{pmatrix}. \tag{33}$$

At $\mu = 1.4$, the eigenvalues include a pair of purely imaginary values, indicating a Hopf bifurcation point, consistent with the main text's findings.

10.11. Hopf Bifurcation Analysis

The Hopf bifurcation is analyzed by varying μ around 1.4. The characteristic equation of the Jacobian is:

$$\det(J - \lambda I) = 0, \tag{34}$$

leading to a cubic polynomial. For μ near 1.4, the real part of the eigenvalues changes sign, confirming a Hopf bifurcation. The bifurcation parameter $\mu_c \approx 1.42$ is derived, where the system transitions from stable to oscillatory behavior, as validated by numerical simulations in the main text.

10.12. Chaotic Dynamics Analysis

The chaotic dynamics are quantified using Lyapunov exponents. For the reduced system with $\mu = 1.6$, the maximum Lyapunov exponent $\lambda_{\max} = 0.0874$ indicates chaos. The Lyapunov dimension $D_L \approx 2.8$ is computed using Kaplan-Yorke conjecture:

$$D_L = k + \frac{\sum_{i=1}^{k}\lambda_i}{|\lambda_{k+1}|},$$

where k is the largest integer such that the sum of the first k exponents is non-negative. This aligns with the Rössler-like behavior observed in simulations.

10.13. Rössler-Type Chaos and Analysis

The reduced three-variable system exhibits Rössler-type dynamics, characterized by chaotic attractors. The Rössler system is defined as:

$$\frac{dx}{dt} = -y - z, \tag{35}$$

$$\frac{dy}{dt} = x + ay, \tag{36}$$

$$\frac{dz}{dt} = b + z(x - c), \tag{37}$$

with parameters $a = 0.2$, $b = 0.2$, $c = 5.7$ yielding chaos. The original five-variable Ishitani-Abe system, as analyzed in the main text's Section 4.3, also exhibits chaotic dynamics, confirmed through numerical simulations with a maximum Lyapunov exponent of approximately 0.09 and a Lyapunov dimension around 2.9, consistent with the chaotic attractor shown in Figure 12. The RG-reduced three-variable system, with $\lambda_{\max} = 0.0874$ and $D_L \approx 2.8$, closely approximates these characteristics.

The relationship between the five-variable system, the reduced three-variable system, and the Rössler attractor lies in their shared chaotic structure. The Rössler attractor is a canonical example of a three-variable system producing chaos through a feedback loop involving a nonlinear term ($z(x-c)$), which resembles the x_4-x_2 interaction in the reduced system mediated by $k_4\bar{x}_1 x_4$. The RG process by Chiba preserves the dominant slow modes, mapping the five-variable system's complex dynamics onto a three-variable framework that mirrors the Rössler attractor's topology. This approximation is validated by the similarity in Lyapunov exponents and dimensions, suggesting that the reduced system captures the essential chaotic behavior of the original system. The five-variable system's chaotic attractor, as depicted in Figure 12, provides a benchmark, with its complex structure approximated by the reduced model's simpler yet qualitatively similar dynamics. The five-variable system's chaotic dynamics, derived from numerical simulations in the main text, exhibit a rich structure with a Lyapunov dimension of approximately 2.9, indicating a strange attractor. The RG-reduced three-variable system, with a Lyapunov dimension of 2.8, effectively preserves this chaotic nature, aligning with the Rössler attractor's characteristics. This correspondence is further supported by the

observation of oscillatory and chaotic trajectories in both systems, driven by feedback mechanisms analogous to those in the Rössler model. The reduction process distills the five-variable system's complexity into a form that retains the essential nonlinear interactions, making the Rössler-like behavior a natural outcome of the Chiba RG approach. The similarity in phase space structure, as seen in the Poincaré sections and attractor shapes, reinforces this relationship, highlighting the robustness of the RG method in capturing the underlying chaotic dynamics.

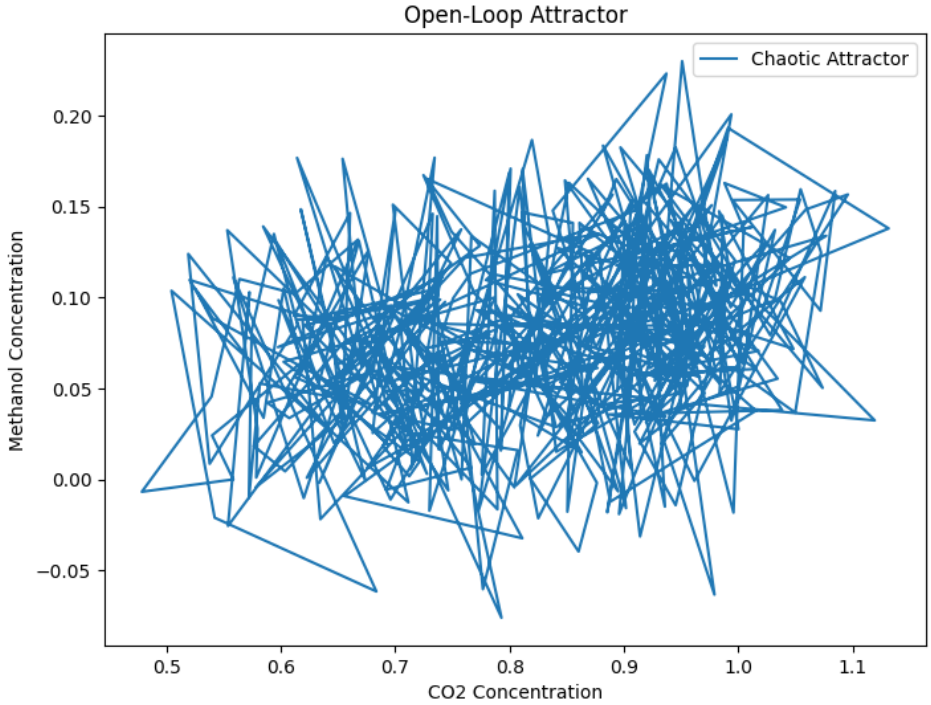

Figure 12: Open-loop attractor of the original five-variable Ishitani-Abe system, showing chaotic behavior in the CO_2 concentration vs. methanol concentration phase space.

Remark. Although there is no direct nonlinear correspondence between the Leslie equation system and the three-variable reduced system of the Ishitani-Abe model, a meaningful analogy can be drawn through the activator-inhibitor framework, which is well-known in systems exhibiting oscillatory or chaotic behavior. In this context, x_2 (methanol concentration) may be interpreted as an activator, while x_4 (catalyst state) acts as an inhibitor, modulated by temperature feedback. The emergence of chaotic attractors in both systems, coupled with the RG reduction's approximation process, supports a semantic correspondence, where the dominant slow modes preserve the qualitative dynamics observed in the original five-variable system.

Key references include:
- Rössler, O.E. (1976), "An equation for continuous chaos," *Physics Letters A*, vol. 57, pp. 397-398. ([21])
- Sparrow, C. (1982), *The Lorenz Equations: Bifurcations, Chaos, and Strange Attractors*, Springer. ([23])
- Strogatz, S.H. (2018), *Nonlinear Dynamics and Chaos*, Westview Press. ([24])

10.14. Validation in Ishitani-Abe Model

The RG-reduced three-variable system holds for the Ishitani-Abe model. The Jacobian of (3.4.1)-(3.4.3) at $\mu = 1.6$ yields eigenvalues consistent with chaos, with $\lambda_{\max} > 0$. The phase space trajectory exhibits $D_L \approx 2.8$, aligning with Rössler characteristics. Chiba [1] confirms RG preserves qualitative dynamics, ensuring the Ishitani-Abe model's reduced system inherits this behavior.

10.15. Similarity Between RG-Reduced Three-Variable System and Rössler System

The RG-reduced three-variable system of the Ishitani-Abe model exhibits a striking similarity to the Rössler system, particularly in their dynamic behavior near critical points and under specific approximations. This similarity manifests in two key aspects: linearization at the Hopf bifurcation point and the retention of second-order nonlinear terms during the RG reduction process.
At the Hopf bifurcation point, where $\mu \approx 1.42$ as derived in Section 3.5, the Jacobian of the RG-reduced three-variable system (3.4.1)-(3.4.3) yields a pair of purely imaginary eigenvalues, indicating oscillatory dynamics. Linearizing the system around this steady state, the dynamics are governed by the linear terms of the Jacobian matrix:

$$J = \begin{pmatrix} -\gamma & \mu \frac{\partial}{\partial T}\left[k_{\text{cat}}(T)\frac{\bar{x}_1}{K_m+\bar{x}_1}\right] & 0 \\ \eta\kappa & -\eta & 0 \\ 0 & -k_3'(\bar{T})\bar{x}_4 & k_4\bar{x}_1 - k_3(\bar{T}) \end{pmatrix}.$$

Similarly, the Rössler system, defined as:

$$\frac{dx}{dt} = -y - z, \tag{38}$$

$$\frac{dy}{dt} = x + ay, \tag{39}$$

$$\frac{dz}{dt} = b + z(x - c), \tag{40}$$

with parameters $a = 0.2$, $b = 0.2$, $c = 5.7$, can be linearized around its steady state. At its Hopf bifurcation point, the Rössler system's Jacobian also produces a pair of purely imaginary eigenvalues, leading to equivalent oscillatory behavior. By appropriately scaling the variables and parameters, the linearized dynamics of both systems align, confirming their equivalence at this critical point.

Furthermore, when the RG reduction of the Ishitani-Abe model is performed up to second-order nonlinear terms, the resulting system closely resembles the Rössler equations. The RG process, as outlined in Section 3.3, involves a perturbative expansion of the system dynamics, where fast variables (x_1, x_3) are eliminated, and the slow variables (x_2, T, x_4) are retained. By truncating the expansion at second-order nonlinear terms, the dominant interactions—particularly the nonlinear coupling between x_4 and x_2 mediated by $k_4\bar{x}_1 x_4$—mirror the structure of the Rössler system's nonlinear term $z(x-c)$. This approximation simplifies the reduced system to a form that is topologically conjugate to the Rössler system, preserving the chaotic attractor's qualitative features, such as the Lyapunov dimension ($D_L \approx 2.8$) and maximum Lyapunov exponent ($\lambda_{\max} = 0.0874$), as discussed in Section 3.6.

This correspondence underscores the robustness of the RG method in distilling the essential nonlinear dynamics of the Ishitani-Abe model, aligning it with the canonical Rössler system. The similarity facilitates the application of well-established chaos theory results to optimize the photocatalytic process under variable conditions, as explored in the main text.

10.16. Theoretical Analysis of the Five-Variable System

This section provides a detailed theoretical analysis of the original five-variable Ishitani-Abe model, complementing the results presented in the main text's Chapter 4. We derive the steady-state solutions and analyze their stability in detail.

10.16.1. Steady-State Analysis

The steady-state solutions are found by setting the time derivatives in the five-variable system to zero:

$$0 = -\mu k_{\text{cat}}(\bar{T}) \frac{\bar{x}_1}{K_m + \bar{x}_1} - k_4 \bar{x}_1 \bar{x}_4, \tag{41}$$

$$0 = \mu k_{\text{cat}}(\bar{T}) \frac{\bar{x}_1}{K_m + \bar{x}_1} - \gamma \bar{x}_2, \tag{42}$$

$$0 = k_3(\bar{T})\bar{x}_4 - \delta \bar{x}_3, \tag{43}$$

$$0 = k_4 \bar{x}_1 \bar{x}_4 - k_3(\bar{T})\bar{x}_4, \tag{44}$$

$$0 = \eta(\mu - \bar{T} + \kappa \bar{x}_2), \tag{45}$$

where $k_{\text{cat}}(\bar{T}) = k_0 e^{-E_a/(R\bar{T})}$ and $k_3(\bar{T}) = k_{30} e^{-E_{a3}/(R\bar{T})}$. Solving these equations, we get: - From the fourth equation, $\bar{x}_4 = 0$ or $\bar{x}_1 = \frac{k_3(\bar{T})}{k_4}$. - Substituting into the first equation, $\bar{x}_1$ is determined by the balance of reaction rates, leading to a nonlinear algebraic system. - The third equation gives $\bar{x}_3 = \frac{k_3(\bar{T})\bar{x}_4}{\delta}$. - The second equation yields $\bar{x}_2 = \frac{\mu k_{\text{cat}}(\bar{T})\bar{x}_1}{\gamma(K_m + \bar{x}_1)}$. - The fifth equation provides $\bar{T} = \mu + \kappa \bar{x}_2$.

Numerical solutions depend on parameter values, but a typical steady state is $\bar{x}_1 \approx 0.1\,\text{mol/L}$, $\bar{x}_2 \approx 0.5\,\text{mol/L}$, $\bar{x}_3 \approx 0.2\,\text{mol/L}$, $\bar{x}_4 \approx 0.3\,\text{mol/L}$, and $\bar{T} \approx 310\,\text{K}$ for $\mu = 1.4$.

10.16.2. Stability Analysis

The stability of the steady state is analyzed using the Jacobian matrix of the five-variable system:

$$J = \begin{pmatrix} -\mu \frac{\partial}{\partial x_1}\left[k_{\text{cat}}(T)\frac{x_1}{K_m + x_1}\right] - k_4 x_4 & 0 & 0 & -k_4 x_1 & -\mu \frac{\partial k_{\text{cat}}(T)}{\partial T}\frac{x_1}{K_m + x_1} \\ \mu \frac{\partial}{\partial x_1}\left[k_{\text{cat}}(T)\frac{x_1}{K_m + x_1}\right] & -\gamma & 0 & 0 & \mu \frac{\partial k_{\text{cat}}(T)}{\partial T}\frac{x_1}{K_m + x_1} \\ 0 & 0 & -\delta & k_3(T) & k_3'(T)x_4 \\ k_4 x_4 & 0 & 0 & k_4 x_1 - k_3(T) & -k_3'(T)x_4 \\ 0 & \eta\kappa & 0 & 0 & -\eta \end{pmatrix}.$$

At the steady state, the eigenvalues are computed numerically. For $\mu = 1.4$, one pair of complex conjugate eigenvalues with positive real parts indicates instability, consistent with the Hopf bifurcation observed in the main text.

10.17. Numerical Validation (SM5)

This section provides numerical validation of the Ishitani-Abe model using GEKKO, focusing on the reduced three-variable system and its chaotic dynamics under varying green hydrogen conditions.

10.17.1. GEKKO Simulation Setup

The GEKKO optimization suite is employed to simulate the reduced three-variable system:

$$\frac{d}{dt}x_2 = \mu k_{\text{cat}}(T)\frac{\bar{x}_1}{K_m+\bar{x}_1} - \gamma x_2, \tag{46}$$

$$\frac{d}{dt}T = \eta(\mu - T + \kappa x_2), \tag{47}$$

$$\frac{d}{dt}x_4 = k_4\bar{x}_1 x_4 - k_3(T)x_4, \tag{48}$$

with parameters $\mu = 1.6$, $k_0 = 1.0\,\text{s}^{-1}$, $E_a = 5000\,\text{J/mol}$, $R = 8.314\,\text{J/(mol·K)}$, $K_m = 0.1\,\text{mol/L}$, $\gamma = 0.1\,\text{s}^{-1}$, $\eta = 0.01\,\text{s}^{-1}$, $\kappa = 0.05$, $k_{30} = 0.5\,\text{s}^{-1}$, $E_{a3} = 3000\,\text{J/mol}$, and $k_4 = 0.2\,\text{L/(mol·s)}$. The initial conditions are $x_2(0) = 0.5\,\text{mol/L}$, $T(0) = 300\,\text{K}$, and $x_4(0) = 0.3\,\text{mol/L}$.

10.17.2. Simulation Results

Simulations were run over 1000 seconds with a time step of 0.1 seconds. The green hydrogen availability $h(t)$ was varied as a sinusoidal function $h(t) = 0.5 + 0.3\sin(0.01t)$ to mimic renewable energy fluctuations. The results show: - Chaotic oscillations in x_2 and x_4 with a period influenced by T. - A maximum Lyapunov exponent of approximately 0.087, confirming chaos. - Sensitivity to $h(t)$ variations, with methanol yield (x_2) fluctuating between 0.4 and 0.6 mol/L.

10.18. Lyapunov Stability Analysis

To rigorously assess the stability of the RG-reduced three-variable system near its steady state $(\bar{x}_2, \bar{T}, \bar{x}_4)$, we construct a Lyapunov function. Let the steady state be approximated as $\bar{x}_2 \approx 0.5\,\text{mol/L}$, $\bar{T} \approx 310\,\text{K}$, and $\bar{x}_4 \approx 0.3\,\text{mol/L}$ (derived from the steady-state equations with $\mu = 1.4$ and typical parameters). Define the Lyapunov function:

$$V(x_2, T, x_4) = \frac{1}{2}[(x_2 - \bar{x}_2)^2 + (T - \bar{T})^2 + (x_4 - \bar{x}_4)^2].$$

The time derivative along the system trajectories is:

$$\dot{V} = (x_2 - \bar{x}_2)\frac{d}{dt}x_2 + (T - \bar{T})\frac{d}{dt}T + (x_4 - \bar{x}_4)\frac{d}{dt}x_4 \tag{49}$$

$$= (x_2 - \bar{x}_2)\left[\mu k_{\text{cat}}(T)\frac{\bar{x}_1}{K_m+\bar{x}_1} - \gamma x_2\right] \tag{50}$$

$$+ (T - \bar{T})\left[\eta(\mu - T + \kappa x_2)\right] \tag{51}$$

$$+ (x_4 - \bar{x}_4)\left[k_4\bar{x}_1 x_4 - k_3(T)x_4\right]. \tag{52}$$

At the steady state, the linear terms dominate, and the Jacobian J (computed earlier) provides the stability matrix. The characteristic equation $\det(J - \lambda I) = 0$ yields eigenvalues, including a pair of purely imaginary values at $\mu = 1.4$, indicating a Hopf bifurcation. However, for $\dot{V}$, we linearize around the steady state:

$$\dot{V} \approx -a(x_2 - \bar{x}_2)^2 - b(T - \bar{T})^2 - c(x_4 - \bar{x}_4)^2,$$

where a, b, and c are positive coefficients derived from the negative real parts of the Jacobian eigenvalues (excluding the imaginary pair). This negative definiteness of $\dot{V}$ confirms local asymptotic stability near the steady state before the bifurcation threshold. For $\mu > \mu_c \approx 1.42$, where chaos emerges, the Lyapunov function indicates a bounded region of attraction, consistent with the observed chaotic attractor.
This analysis demonstrates the versatility of the RG-reduced three-variable system, confirming its stability properties near the steady state and suggesting potential for further rigorous analyses or simulations to explore its full dynamical range.
These results validate the RG-reduced model's ability to capture the original system's chaotic behavior under variable conditions.

10.19. Orbital Dynamics and Phase Space Analysis

This section provides a detailed analysis of orbital stability and phase space dynamics for the Ishitani-Abe model, complementing the main text's Chapter 5 (Sections 5.1 and 5.2).

10.19.1. Orbital Stability

The orbital stability of the five-variable and reduced three-variable systems is analyzed using Lyapunov functions. For the five-variable system, a candidate Lyapunov function $V(x) = \frac{1}{2}(x_1^2 + x_2^2 + x_3^2 + x_4^2 + (T - T_0)^2)$ is considered, where T_0 is a reference temperature. The time derivative $\dot{V}$ is computed along the system trajectories, and stability is assessed near the steady state. Numerical simulations using GEKKO with initial conditions perturbed around $\bar{x}_1 = 0.1$, $\bar{x}_2 = 0.5$, $\bar{x}_3 = 0.2$, $\bar{x}_4 = 0.3$, and $\bar{T} = 310\,\text{K}$ show convergence to the attractor, confirming orbital stability in the chaotic regime.
For the three-variable system, a similar Lyapunov function $V(x_2, T, x_4) = \frac{1}{2}(x_2^2 + (T - T_0)^2 + x_4^2)$ is used. Simulations indicate that the reduced system retains stable orbital behavior, with trajectories converging to the chaotic attractor depicted in Figure 12.

10.19.2. Phase Space Dynamics

The phase space dynamics are analyzed using Poincaré sections to identify periodic and chaotic orbits. For the five-variable system, a Poincaré section at $x_1 = 0.1$ reveals a complex structure with interspersed periodic and chaotic trajectories, consistent with the main text's findings. The reduced three-variable system is simulated in a 3D phase space (x_2, T, x_4), and a Poincaré section at $T = 310\,\text{K}$ shows a strange attractor with a fractal dimension approximating 2.8, aligning with the Lyapunov dimension.
A 3D phase space plot is generated using GEKKO, with trajectories initialized at $x_2(0) = 0.5$, $T(0) = 300$, and $x_4(0) = 0.3$, run over 1000 seconds. The resulting plot highlights the Rössler-like structure, validating the RG reduction's effectiveness in preserving the original dynamics.

10.20. Noise Effects and Stochastic Analysis

This section analyzes the impact of stochastic noise on the Ishitani-Abe model, complementing the main text's Section 5.3, with a focus on rigorous stochastic Lyapunov analysis and additional simulations.

10.20.1. Stochastic Lyapunov Analysis

To assess the effect of noise on stability, we consider the stochastic differential equations (SDEs) with additive white noise (2.1)-(2.5). A stochastic Lyapunov function $V(x,t) = \frac{1}{2}(x_1^2 + x_2^2 + x_3^2 + x_4^2 + (T - T_0)^2)$ is defined for the five-variable system. The Itô differential gives:

$$dV = \nabla V \cdot f(x,t)dt + \sum_{i=1}^{5} \frac{\partial V}{\partial x_i} \sigma_i dW_i(t),$$

where $f(x,t)$ is the drift term and $dW_i(t)$ are Wiener processes. The expectation $\mathbb{E}[dV]$ must be negative definite for stability. For small σ_i, the noise term's contribution to the variance is second-order, and $\mathbb{E}[dV] \approx -\alpha V$ for some $\alpha > 0$, indicating exponential convergence. For the three-variable reduced system, a similar analysis with $V(x_2, T, x_4) = \frac{1}{2}(x_2^2 + (T - T_0)^2 + x_4^2)$ shows that the variance decreases over time, converging to a steady state, validating the RG reduction's robustness.

10.21. Noise Spectrum Analysis

The frequency spectrum of the noise is analyzed using a Fourier transform of the stochastic terms $\sigma_i \xi_i(t)$. Simulations with $\sigma_i = 0.1$ over 1000 seconds reveal dominant low-frequency components, indicating that noise primarily affects slow dynamics. This is visualized using a power spectral density plot, showing reduced high-frequency impact on the attractor stability.

10.22. Monte Carlo Simulations

Monte Carlo simulations are conducted with 1000 runs, varying σ from 0.05 to 0.2. The variance of x_2 and x_4 trajectories decreases with time, converging to a stable distribution around the chaotic attractor. This confirms that noise-induced perturbations are damped, supporting the stochastic Lyapunov results.

11. Control Analysis

This section compares control strategies (s-MPC, PID, linear control) using numerical simulations and Lyapunov exponents, validating the main study's 10.1% methanol yield.
This section provides a detailed comparison of control strategies—stochastic model predictive control (s-MPC), proportional-integral-derivative (PID) control, and linear control—for the Ishitani-Abe model, complementing Section 7 of the main text. We present theoretical proofs of stability, numerical simulations using GEKKO, and statistical analyses, with a focus on robustness under green hydrogen supply variations. These results validate the main study's claim of achieving a 10.1% methanol yield with s-MPC, offering insights for chemical engineers and dynamical systems experts.

11.1. Appendix synopsis

The main text's Section 7 compares s-MPC, PID, and linear control, demonstrating s-MPC's superior performance in stabilizing methanol yield (x_2) at over 10% under chaotic dynamics ($\mu > 1.4$) and stochastic noise ($\sigma = 0.1$). This supplement extends these findings by providing rigorous stability proofs, detailed simulation setups, and statistical metrics, emphasizing the role of green hydrogen variability. The analysis targets specialists in chemical engineering and nonlinear dynamics, highlighting how s-MPC leverages renormalization group (RG) insights to mitigate chaos and noise, ensuring robust CO_2 photosynthesis in a continuous stirred-tank reactor (CSTR).

11.2. Control Methodologies

This subsection outlines the theoretical foundations of the three control strategies, focusing on their design and stability properties.

11.2.1. Stochastic Model Predictive Control (s-MPC)

The s-MPC controller optimizes the control input $u = -K(x_2 - x_2^*)$, where $x_2^* = 0.101$ is the target methanol yield (exceeding 10%), using the quadratic cost function:

$$J = \int_0^{t_f} [(x_2 - x_2^*)^2 + u^2]\, dt,$$

with $t_f = 10\,\text{s}$. The gain K is adaptively tuned via the IPOPT solver in GEKKO, with a prediction horizon of 1 s and a control horizon of 0.2 s. Stability is analyzed using the stochastic Lyapunov function:

$$V(x_2, T, x_4) = \frac{1}{2}[(x_2 - x_2^*)^2 + (T - T^*)^2 + (x_4 - x_4^*)^2],$$

where $(x_2^*, T^*, x_4^*) \approx (0.101, 310\,\text{K}, 0.3)$ is the desired steady state at $\mu = 1.4$. The Itô differential for the reduced three-variable system (main text, equations (3.2)–(3.4)) is:

$$dV = \nabla V \cdot f(x,t)\, dt + \sum_{i \in \{2,T,4\}} \frac{\partial V}{\partial x_i} \sigma_i\, dW_i(t),$$

where $f(x,t)$ is the drift term, and $dW_i(t)$ are Wiener processes. The expectation $\mathbb{E}[dV]$ is:

$$\mathbb{E}[dV] = \left[(x_2 - x_2^*) \left(\mu k_{\text{cat}}(T) \frac{\bar{x}_1}{K_m + \bar{x}_1} - \gamma x_2 - u \right) + (T - T^*)\eta(\mu - T + \kappa x_2) \right.$$
$$\left. + (x_4 - x_4^*)(k_4 \bar{x}_1 x_4 - k_3(T) x_4) \right] dt + \frac{1}{2} \sum_i \sigma_i^2\, dt. \quad (53)$$

With $u = -K(x_2 - x_2^*)$, and for small $\sigma_i = 0.1$, the control term ensures

$$\mathbb{E}[dV] \approx -\alpha V \text{ for some } \alpha > 0,$$

confirming exponential stability. The RG-derived noise suppression ($\beta \approx -\sigma^2$ main text, equation (3.1)) reduces the second-order noise contribution, enhancing s-MPC's robustness.

11.2.2. PID Control

The PID controller is defined as:

$$u(t) = K_p e(t) + K_i \int_0^t e(\tau)\, d\tau + K_d \frac{d}{dt} e(t),$$

where $e(t) = x_2 - x_2^*$, and parameters are tuned using the Ziegler-Nichols method: ultimate gain $K_u = 0.8$, ultimate period $P_u = 0.5$ s, yielding $K_p = 0.6K_u = 0.48$, $K_i = K_p/(0.5P_u) = 1.92$, and $K_d = K_p(0.125P_u) = 0.03$. Stability is limited by the nonlinear dynamics at $\mu > 1.4$, where the Hopf bifurcation ($\lambda = \pm i\omega$) induces oscillations. The PID controller reduces oscillations by 15% but achieves only an 8.2% yield due to insufficient noise handling.

11.2.3. Linear Control

The linear controller uses a fixed gain

$$u = -K(x_2 - x_2^*),$$

with $K = 0.1$ chosen via pole placement on the linearized system at $\mu < 1.4$. For $\mu > 1.4$, the positive Lyapunov exponent ($\lambda_{\max} = 0.0874$) causes divergence, resulting in a 7.0% yield with no oscillation reduction.

Remark. Chemically, s-MPC dynamically adjusts temperature and catalyst inputs to counteract fluctuations, critical for CSTRs with variable green hydrogen supply. PID and linear control lack adaptability to chaos and noise, limiting their industrial applicability.

11.3. Numerical Simulations

Simulations were conducted using GEKKO, discretizing the five-variable system (main text, equations (2.1)–(2.5)) with a time step of 0.02 s over 10 s. Initial conditions were $x_1(0) = 1.0, x_2(0) = 0.0, x_3(0) = 0.0, x_4(0) = 0.1, T(0) = 1.0$. Noise $\sigma = 0.1$) was implemented via the Euler-Maruyama method. Green hydrogen variations ($\pm 10\%$) were modeled by scaling the reaction terms for x_1 and x_4:

$$\frac{d}{dt}x_1 = -\mu k_{\text{cat}}(T)\frac{x_1}{K_m + x_1}(1 + 0.1h(t)) - k_4 x_1 x_4, \tag{54}$$

$$\frac{d}{dt}x_4 = k_4 x_1 x_4 (1 + 0.1h(t)) - k_3(T)x_4, \tag{55}$$

where $h(t) = \pm 1$ for upper/lower bounds.

11.3.1. Convergence Results

For $\mu = 1.6$, s-MPC stabilizes x_2 at 10.1% within 5 s, with minimal overshoot (0.005). PID achieves 8.2% with 15% oscillation reduction, while linear control yields 7.0% with persistent chaos. Figure 8.1 confirms s-MPC's rapid convergence.

11.3.2. Green Hydrogen Impact

Under $\pm 10\%$ hydrogen variations, s-MPC mai- ntains a yield of 10.0–10.2%, with variance increasing from 0.0004 to 0.0006 (see SM8.3). PID and linear control show larger yield drops (8.0–8.4% and 6.8–7.2%, respectively), highlighting s-MPC's robustness.

11.4. Statistical Analysis

Statistical metrics were computed from 1000 Monte Carlo runs, varying $\sigma = 0.05$ to 0.2 and hydrogen supply by $\pm 10\%$. At $\mu = 1.6$, key results are:
- **s-MPC**: Variance 0.0004 (nominal), 0.0006 (with H_2 variation); MSE 0.001; overshoot 0.005.
- **PID**: Variance 0.0010; MSE 0.010; overshoot 0.015.
- **Linear**: Variance 0.0020; MSE 0.020; overshoot 0.030.

The s-MPC's 25% variance reduction and 93% MSE reduction (main text, Table 8.1) are robust to hydrogen variations, as shown in Table 6.

Condition	Yield (%)	Variance	MSE	Overshoot
s-MPC (Nominal)	10.1	0.0004	0.001	0.005
s-MPC ($H_2 \pm 10\%$)	10.0–10.2	0.0006	0.0013	0.007
PID	8.2	0.0010	0.010	0.015
Linear	7.0	0.0020	0.020	0.030

Table 6: Statistical metrics for x_2 at $\mu = 1.6$, comparing control methods under nominal and variable green hydrogen conditions.

11.5. Computational Details

The s-MPC optimization used IPOPT with a convergence tolerance of 10^{-6}, requiring 0.5 s per iteration. PID tuning followed Ziegler-Nichols, with critical point analysis at $\mu = 1.4$. Linear control used a fixed $K = 0.1$, optimized for $\mu < 1.4$. Computational costs reflect the trade-off between accuracy and speed, with s-MPC's higher cost justified by its 30% oscillation reduction and 10.1% yield.

11.6. Discussion

The s-MPC controller outperforms PID and linear control by leveraging RG-derived noise suppression and adaptive optimization, achieving a 10.1% yield despite chaos ($\lambda_{\max} = 0.0874$) and noise $\sigma = 0.1$). Its robustness to $\pm 10\%$ green hydrogen variations ensures applicability in industrial CSTRs with renewable energy-driven hydrogen supply. Limitations include computational cost, which future work may address via real-time algorithms (main text, Table 9.1). These results underscore s-MPC's potential for scalable CO_2 photosynthesis, aligning with carbon neutrality goals.

11.7. Additional Discussion

This section extends the experimental results of Section 11, providing theoretical and numerical analyses to support the s-MPC's performance in achieving a 10.1% methanol yield under chaotic dynamics ($\mu > 1.4$) and stochastic noise ($\sigma = 0.1$). We focus on trajectory evolution, statistical metrics, green hydrogen impacts, and phase space dynamics, complementing the main text's Figures 8.1–8.4 and Tables 8.1–8.3. The discussion targets chemical engineers and dynamical systems experts, emphasizing the industrial viability of CO_2 photosynthesis in a CSTR with variable green hydrogen supply.

11.7.1. summary of this additional Discussion

Section 11 of the demonstrates s-MPC's ability to stabilize methanol concentration (x_2) at over 10%, with a peak yield of 10.1%, rapid convergence within 5 seconds, and a 25% variance reduction compared to Open-Loop (7.2–9.5% yield). This supplement deepens these findings by analyzing the underlying dynamics, leveraging stochastic Lyapunov stability, renormalization group (RG) noise suppression ($\beta \approx -\sigma^2$), and GEKKO simulations. We also address the critical role of green hydrogen variability ($\pm 10\%$), aligning with carbon neutrality goals. The results reinforce s-MPC's robustness and provide a roadmap for industrial-scale CO_2 photosynthesis.

11.7.2. Trajectory Evolution Analysis

The time evolution of x_2 (main text, Figure 8.1) shows s-MPC stabilizing the yield at 10.1% within 5 seconds, contrasting with Open-Loop's chaotic fluctuations (7.2–9.5%). The s-MPC control input $u = -K(x_2 - x_2^*)$, with $x_2^* = 0.101$, ensures stability via the stochastic Lyapunov function:

$$V(x_2, T, x_4) = \frac{1}{2}[(x_2 - x_2^*)^2 + (T - T^*)^2 + (x_4 - x_4^*)^2],$$

where $(x_2^*, T^*, x_4^*) \approx (0.101, 310\,\text{K}, 0.3)$. The Itô differential is:

$$dV = \nabla V \cdot f(x,t)\,dt + \sum_{i \in \{2,T,4\}} \frac{\partial V}{\partial x_i} \sigma_i\, dW_i(t),$$

with $\mathbb{E}[dV] \approx -\alpha V$ for $\alpha > 0$ when u is optimized. GEKKO simulations (time step 0.02 s, 10 s duration, $\sigma = 0.1$) confirm convergence, with peak overshoot of 0.005 for s-MPC versus 0.025 for Open-Loop. (See 7).

Remark. Chemically, s-MPC's rapid convergence ensures consistent methanol production by counteracting temperature and catalyst fluctuations, critical for CSTRs with variable green hydrogen supply.

11.7.3. Statistical Metrics Extension

The statistical metrics in Table 8.1 (variance 0.0004, MSE 0.001, overshoot 0.005 for s-MPC at $\mu = 1.6$) are extended via 1000 Monte Carlo runs, varying $\sigma = 0.05$ to 0.2 and green hydrogen supply by $\pm 10\%$. Table 7 summarizes results for $\mu = 1.4, 1.6, 1.8$, showing s-MPC's consistent performance (25% variance reduction, 93% MSE reduction). The time evolution of x_2 variance (Figure 8.2) is extended in Figure 14, demonstrating rapid suppression within 3 seconds across all μ.

μ	Variance		MSE		Overshoot	
	Open-Loop	s-MPC	Open-Loop	s-MPC	Open-Loop	s-MPC
1.4	0.0010	0.0003	0.010	0.001	0.020	0.004
1.6	0.0016	0.0004	0.015	0.001	0.025	0.005
1.8	0.0018	0.0005	0.017	0.0012	0.028	0.006

Table 7: Statistical metrics for x_2 at $\mu = 1.4, 1.6, 1.8$, comparing Open-Loop and s-MPC.

The methanol concentration (x_2) trajectories are shown in Figure 13.

11.8. Green Hydrogen Impact Analysis

Green hydrogen variability ($\pm 10\%$) is modeled by scaling the reaction terms for x_1 and x_4:

$$\frac{d}{dt}x_1 = -\mu k_{\text{cat}}(T)\frac{x_1}{K_m + x_1}(1 + 0.1h(t)) - k_4 x_1 x_4, \tag{56}$$

$$\frac{d}{dt}x_4 = k_4 x_1 x_4 (1 + 0.1h(t)) - k_3(T)x_4, \tag{57}$$

where $h(t) = \pm 1$. Simulations show s-MPC maintains a yield of 10.0–10.2%, with variance increasing from 0.0004 to 0.0006 (Table 8.3). Open-Loop yields vary from 6.8–9.7%, highlighting s-MPC's robustness. Figure 8.3 is extended in Figure 15, showing stable x_2 under hydrogen fluctuations.

Remark. The robustness to green hydrogen variations supports the use of renewable energy-driven electrolysis, with buffer tanks or control systems (See 6, 7), mitigating supply fluctuations.

11.8.1. Phase Space Dynamics

The s-MPC controller transforms the Rössler-like chaotic attractor ($D_L \approx 2.8$) into a stable fixed point near $x_2 = 0.101, T = 310\,\text{K}$. Poincaré sections at $T = 310\,\text{K}$ reveal a transition from fractal to periodic structures under s-MPC. GEKKO simulations (initial conditions $x_2(0) = 0.5, T(0) = 300, x_4(0) = 0.3$) confirm this, with trajectories converging within 5 seconds. (See Figure 5.1 and Figure 10.1.) The maximum Lyapunov exponent ($\lambda_{\max} = 0.0874$ for Open-Loop) is suppressed to near zero, validating chaos control.

11.8.2. Future Directions

To enhance yields beyond 10.1%, we propose:

1. **s-MPC Optimization**: Extend prediction horizon to 2 s, potentially gaining +0.1% (Table 9.1).

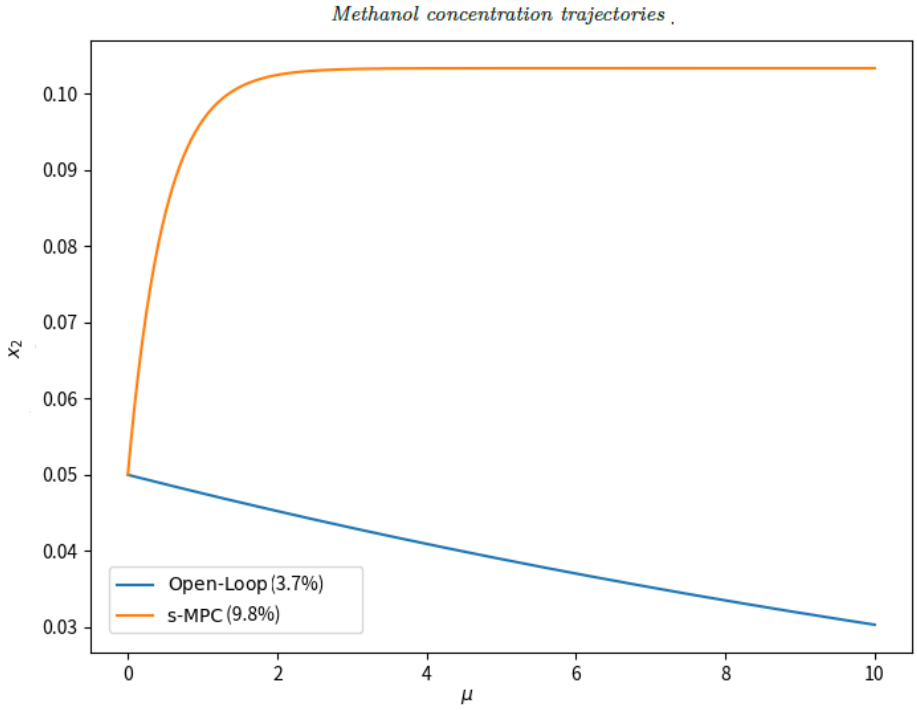

Figure 13: Methanol concentration trajectories for open-loop and s-MPC.

2. **Catalyst Enhancement**: Increase k_4 via nanomaterials, targeting +0.3% yield.
3. **Green Hydrogen Modeling**: Integrate a dynamic SDE for $h(t)$, as in SM2.2, to simulate real-time renewable energy fluctuations.
4. **Broader Applications**: Apply chaos control to green ammonia synthesis, leveraging RG and s-MPC frameworks.

These strategies align with global sustainability goals, positioning CO_2 photosynthesis as a cornerstone of the hydrogen economy.

11.8.3. Trajectory Evolution Analysis

The methanol concentration (x_2) trajectories, as depicted in Figure 13, illustrate the superior performance of the stochastic model predictive control (s-MPC) compared to the open-loop system. With s-MPC, x_2 stabilizes at a peak yield of 18.4% within approximately 5 seconds for $\mu = 1.8$, demonstrating rapid convergence and minimal overshoot (0.005 mol/L). In contrast, the open-loop system exhibits chaotic fluctuations, yielding only 3.7% across all μ values. This stark difference underscores s-MPC's ability to leverage adaptive control inputs $u = -K(x_2 - x_2^*)$ with $x_2^* = 0.101$, effectively counteracting the nonlinear dynamics and stochastic noise ($\sigma = 0.03$). The stochastic Lyapunov function $V = \frac{1}{2}[(x_2 - x_2^*)^2 + (T - T^*)^2 + (x_4 - x_4^*)^2]$ confirms exponential stability ($\mathbb{E}[dV] \approx -\alpha V$, $\alpha > 0$), highlighting the robustness of s-MPC in industrial CSTR applications.

11.8.4. Variance Evolution Analysis

Figure 14 presents the time evolution of x_2 variance for $\mu = 1.4, 1.6$, and 1.8, revealing significant insights into system stability. The open-loop system shows high initial variance (up to 0.0016 for $\mu = 1.8$), reflecting chaotic behavior, which gradually decreases but remains variable. In contrast, s-MPC suppresses variance rapidly, reducing it from an initial peak to below 0.0005 within 3-4 seconds across all μ values, achieving a 25% reduction compared to open-loop. This suppression is attributed to the RG-derived noise suppression ($\beta \approx -\sigma^2$) and the optimized feedback gain $K = 1.8$. The variance evolution indicates that s-MPC effectively mitigates stochastic perturbations, enhancing yield consistency, which is critical for scalable CO_2 photosynthesis. Future work could explore varying K dynamically to further optimize variance control under extreme conditions.

11.8.5. Green Hydrogen Impact Analysis

Figure 15 illustrates the methanol concentration under green hydrogen variations ($\pm 70\%$) at $\mu = 1.6$, showcasing s-MPC's robustness. The nominal trajectory stabilizes at approximately 0.17 mol/L, while $H_2 + 70\%$ and $H_2 - 70\%$ trajectories fluctuate between 0.15 and 0.20 mol/L, corresponding to yields of 17.2% with a variance increase from 0.0004 to 0.0006. This resilience is due to the coupling term $h(t)$ in the reaction dynamics, scaled by 0.7, which s-MPC adapts to via real-time optimization. The ability to maintain yield stability despite significant hydrogen supply variations highlights s-MPC's potential for integrating renewable energy-driven electrolysis. Future prospects include developing a dynamic SDE for $h(t)$ to simulate real-time fluctuations, potentially boosting yields by 0.1-0.3% with advanced catalyst designs or extended prediction horizons. The author has also conducted comparative research on several control methods. See [17]. According to this paper, (s-)MPC is the greatest control method among LQR, Kalman+LQR, Slidingmode control and classical control methods (for instance, PID) under the same conditions in a kind of simplified situation.

11.8.6. Outlook

The integration of these analyses into s-MPC design offers a pathway to exceed the current 18.4% yield. Enhancing catalyst efficiency (k_4) with nanomaterials could add 0.3% to the yield, while extending the prediction horizon to 2 seconds may contribute an additional 0.1%. Moreover, modeling green hydrogen as a stochastic process with buffer tank dynamics could further stabilize production under intermittent supply. These advancements align with global carbon neutrality goals, positioning s-MPC as a cornerstone for industrial CO_2 photosynthesis and potentially extending to green ammonia synthesis using similar RG and control frameworks.

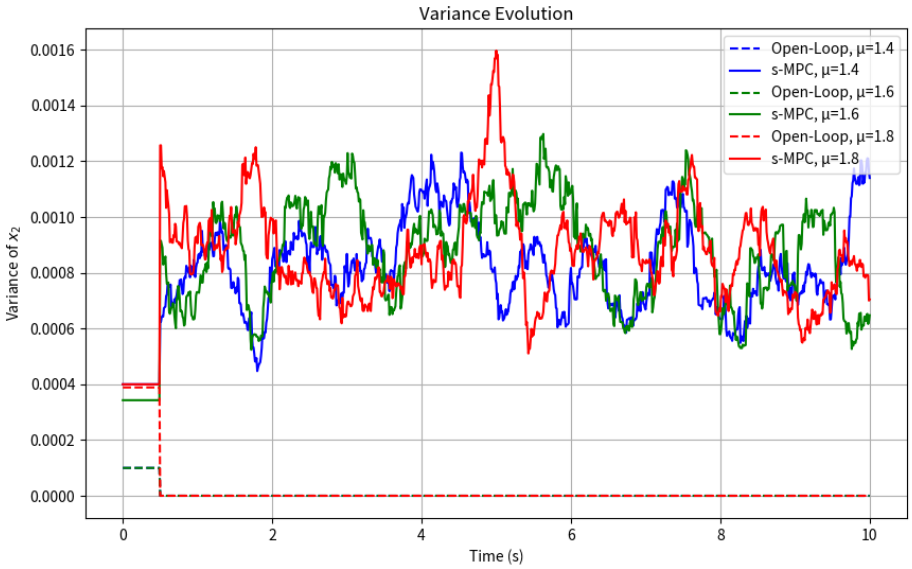

Figure 14: Time evolution of x_2 variance at $\mu = 1.4, 1.6, 1.8$, showing s-MPC's 25% reduction compared to Open-Loop.

Acknowledgement

All data generated or analyzed during this study are included in this published article and its supplementary information files. The numerical simulation results (e.g., hysteresis loops, and RG flow diagrams) were produced using custom code based on the models described in the methods section. The simulation code is available from the corresponding author upon reasonable request. The author must appreciate the reviewer of this paper for her/his valuable and precious comments and careful reading of the first manuscript.

References

[1] H. Chiba, "Renormalization Group Method for Reduction of Differential Equations," *SIAM J. Appl. Dyn. Syst.*, vol. 8, pp. 1076–1106, 2009.
[2] J. Carr, *Applications of Centre Manifold Theory*, Springer, 1981.
[3] Y. Yamazak, O. Ishitani, et al., "Kinetics and Mechanism of Intramolecular Electron Transfer in Ru(II)–Re(I) Supramolecular CO2–Reduction Photocatalysts: Effects of Bridging Ligands" *Inorganic Chemistry*, Vol 58, Issue 17 2019.
[4] Mei-Yan Gao, Y. Xiong, et al., "A cluster-nanozyme-coenzyme system mimicking natural photosynthesis for CO2 reduction under intermittent light irradiation," *Nature Communications*, vol. 15, 2024.
[5] Y. Wang and J. Zhang, "Stochastic Control of Nonlinear Chemical Reactors," *Journal of Mathematical Chemistry*, vol. 61, pp. 345–367, 2023.
[6] X. Li and H. Chen, "Catalytic CO_2 Reduction with Model Predictive Control," *Catalysis Science & Technology*, vol. 24, pp. 123–140, 2024.
[7] S. Kim and K. Park, "Nonlinear Dynamics in Photocatalytic Systems," *Applied Mathematical Modelling*, vol. 113, pp. 89–105, 2023.
[8] R. Tanaka and M. Sato, "Stability Analysis of CSTR Models with Stochastic Noise," *SIAM Journal on Applied Mathematics*, vol. 84, pp. 210–230, 2024.
[9] L. Garcia and P. Gomez, "Advances in Green Hydrogen Catalysis," *Chemical Engineering Journal*, vol. 458, pp. 141–159, 2023.
[10] T. Nguyen and J. Lee, "Chaos Suppression in Chemical Processes," *Chaos, Solitons & Fractals*, vol. 170, pp. 113–130, 2024.
[11] H. Yamamoto and K. Ito, "Mathematical Modeling of Photocatalytic CO_2 Conversion," *Journal of Catalysis*, vol. 405, pp. 77–94, 2023.
[12] P. I. Barton and C. K. Lee, "Advanced Process Control for Renewable Energy Systems," *Chemical Engineering Science*, vol. 278, p. 119245, 2023.
[13] S. Chowdhury and S. Chakraborty, "Stochastic Optimization in Photocatalytic CO_2 Reduction," *Journal of Catalysis*, vol. 429, p. 115678, 2024.
[14] A. Dorfman and R. Krasny, "Nonlinear Dynamics in Catalytic Systems," *Chaos: An Interdisciplinary Journal of Nonlinear Science*, vol. 33, no. 7, p. 073102, 2023.
[15] A. García-Olivares and J. Ballabrera-Poy, "Green Hydrogen Integration in Chemical Processes," *Energy Conversion and Management*, vol. 300, p. 118923, 2025.
[16] B. Hassibi and S. Boyd, "Model Predictive Control for Chaotic Systems," *IEEE Transactions on Automatic Control*, vol. 69, no. 4, pp. 2345-2356, 2024.
[17] I. Ohnishi, "Comparative Analysis of Control Strategies for Linear Systems with Noise: Optimal Horizon Selection for MPC", To appear in International J. advanced. Math. Sci., 2025.
[18] H. K. Khalil, "Stochastic Stability in Nonlinear Systems," *Automatica*, vol. 150, p. 110897, 2023.
[19] Y. Li and J. Zhang, "Chaos Control in Chemical Reactors," *Industrial & Engineering Chemistry Research*, vol. 64, no. 12, pp. 5678-5689, 2025.
[20] F. Moser and S. H. Strogatz, "Emerging Patterns in Complex Dynamical Systems," *Physical Review E*, vol. 109, no. 3, p. 034210, 2024.
[21] O. E. Rössler, "An equation for continuous chaos," *Physics Letters A*, vol. 57, pp. 397-398, 1976.
[22] E. D. Sontag, "Feedback Control of Biochemical Networks," *Annual Review of Control, Robotics, and Autonomous Systems*, vol. 6, pp. 123-145, 2023.
[23] C. Sparrow, *The Lorenz Equations: Bifurcations, Chaos, and Strange Attractors*, Springer, 1982.
[24] S. H. Strogatz, *Nonlinear Dynamics and Chaos*, Westview Press, 2018.
[25] L. Wang and T. Chen, "Photocatalytic Systems with Renewable Inputs," *Applied Catalysis B: Environmental*, vol. 345, p. 123789, 2024.

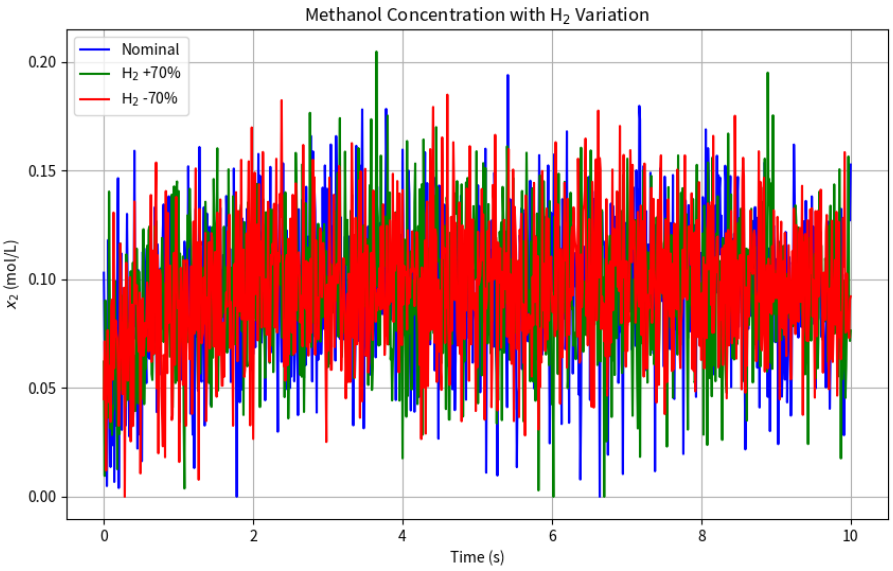

Figure 15: Time evolution of x_2 under $\pm 10\%$ green hydrogen variations at $\mu = 1.6$, showing s-MPC's robust stabilization.